

## ARTICLE OPEN

Single-material MoS<sub>2</sub> thermoelectric junction enabled by substrate engineering

Mohammadali Razeghi<sup>1</sup>, Jean Spiece<sup>1,2</sup>, Oğuzhan Oğuz<sup>1</sup>, Doruk Pehlivanoğlu<sup>3</sup>, Yubin Huang<sup>1,2</sup>, Ali Sheraz<sup>1,3</sup>, Uğur Başçı<sup>3</sup>, Phillip S. Dobson<sup>4</sup>, Jonathan M. R. Weaver<sup>4</sup>, Pascal Gehring<sup>1,2</sup> and T. Serkan Kasirga<sup>1,3</sup>✉

To realize a thermoelectric power generator, typically, a junction between two materials with different Seebeck coefficients needs to be fabricated. Such differences in Seebeck coefficients can be induced by doping, which renders it difficult when working with two-dimensional (2d) materials. However, doping is not the only way to modulate the Seebeck coefficient of a 2d material. Substrate-altered electron–phonon scattering mechanisms can also be used to this end. Here, we employ the substrate effects to form a thermoelectric junction in ultrathin, few-layer MoS<sub>2</sub> films. We investigated the junctions with a combination of scanning photocurrent microscopy and scanning thermal microscopy. This allows us to reveal that thermoelectric junctions form across the substrate-engineered parts. We attribute this to a gating effect induced by interfacial charges in combination with alterations in the electron–phonon scattering mechanisms. This work demonstrates that substrate engineering is a promising strategy for developing future compact thin-film thermoelectric power generators.

npj 2D Materials and Applications (2023)7:36; <https://doi.org/10.1038/s41699-023-00406-z>

## INTRODUCTION

In ultrathin materials with large surface-to-bulk ratio, interactions with the substrate can have a strong impact on the material's properties<sup>1–6</sup>. It is therefore important to understand this so-called substrate effect, especially in order to optimize the reliability of future devices based on two-dimensional (2d) semiconducting materials. As an example, the choice of substrate for mono- and few-layer MoS<sub>2</sub> has been shown to strongly affect its Raman modes and photoluminescence (PL)<sup>7</sup>, electronic<sup>8</sup>, and thermal transport<sup>9</sup> properties. In the following, we predict that a thermoelectric junction with a Seebeck coefficient difference of tens of  $\mu\text{V K}^{-1}$  can be fabricated when connecting regions of suspended MoS<sub>2</sub> to supported regions based on the experimental evidence reported before<sup>9</sup>.

We assume that the Seebeck coefficient  $S$  in thermal equilibrium is composed of contributions from the energy-dependent diffusion ( $S_N$ ), scattering ( $S_\tau$ ) and the phonon-drag ( $S_{pd}$ ), so that  $S = S_N + S_\tau + S_{pd}$ <sup>9,10</sup>. Here,  $S_N$  and  $S_\tau$  terms can be written from the Mott relation assuming that MoS<sub>2</sub> is in the highly conductive state and electrons are the majority carriers:

$$S_\tau = -\frac{\pi^2 k_B^2 T}{3e} \left. \frac{\partial \ln \tau}{\partial E} \right|_{E=E_F} \quad \text{and} \quad S_N = \pm \frac{k_B}{e} \left[ \frac{E_F - E_C}{k_B T} - \frac{(r+2)F_{r+1}(\eta)}{(r+1)F_r(\eta)} \right] \quad (1)$$

where  $T$  is the temperature,  $k_B$  is the Boltzmann constant,  $e$  is the electron's charge,  $\tau$  is the relaxation time,  $E_F$  is the Fermi energy,  $E_C$  is the conduction band edge energy,  $r$  is scattering parameter and  $E$  is the energy.  $F_m(\eta)$  is the  $m$ -th order Fermi integral<sup>11</sup>. In the 2d limit,  $\tau$  is energy independent; thus  $S_\tau$  is zero.  $S_{pd}$  term can be estimated from the theory of phonon-drag in semiconductors in the first order as  $S_{pd} = -\frac{\beta v_p l_p}{\mu T}$  where  $v_p$  and  $l_p$  are the group velocity and the mean free path of a phonon,  $\beta$  is a parameter to modify the electron–phonon interaction strength and ranges from 0 to 1, and  $\mu$  is the electron mobility, respectively<sup>10</sup>. Importantly,  $l_p$

and  $\mu$  are heavily affected by the presence of a substrate<sup>12</sup>, which implies that the  $S_{pd}$  term gets strongly modified when the MoS<sub>2</sub> flake is suspended. As a result, a thermoelectric junction can be formed on MoS<sub>2</sub> by locally modifying the supporting substrate.

In this work, we employ the substrate effect to enable completely new functionalities in a 2d semiconductor device. To this end, we engineer the substrate that atomically thin MoS<sub>2</sub> is deposited on. Using a combination of scanning photocurrent microscopy (SPCM) along with scanning thermal microscopy (SThM) we demonstrate that substrate engineering is a powerful way to build a thermoelectric junction.

## RESULTS AND DISCUSSION

Scanning photocurrent microscopy on substrate-engineered MoS<sub>2</sub>

Based on the calculation outlined in the Introduction, we find that for suspended MoS<sub>2</sub> at room temperature  $S_{pd} \approx -100 \mu\text{V K}^{-1}$  and for MoS<sub>2</sub> on SiO<sub>2</sub> at room temperature  $S_{pd} \approx -230 \mu\text{V K}^{-1}$ . Similarly,  $S_N$  is heavily influenced by the presence or absence of the substrate as electron density depends on the interfacial Coulomb impurities and short-ranged defects<sup>11–17</sup>. We estimate that that for MoS<sub>2</sub>,  $S_N$  ranges from  $-400 \mu\text{V K}^{-1}$  to  $-200 \mu\text{V K}^{-1}$  for carrier concentrations ranging from  $10^{12} \text{ cm}^{-2}$  (suspended few-layer MoS<sub>2</sub>) to  $3 \times 10^{13} \text{ cm}^{-2}$  (SiO<sub>2</sub> supported few layer MoS<sub>2</sub>)<sup>11,18,19</sup>. As a result, a substrate-engineered thermoelectric junction with a Seebeck coefficient difference of  $\Delta S \approx 70 \mu\text{V K}^{-1}$  can be formed along the MoS<sub>2</sub> flake (see Fig. 1a and Supplementary Note 1).

To test this hypothesis, we fabricated substrate-engineered MoS<sub>2</sub> devices by mechanical exfoliation and dry transfer<sup>20</sup> of atomically thin MoS<sub>2</sub> flakes on substrates (sapphire or oxidized silicon) with pre-patterned trenches/holes formed by focused ion beam (FIB). We contacted the flakes with Indium needles<sup>21–23</sup>,

<sup>1</sup>Bilkent University UNAM—Institute of Materials Science and Nanotechnology, Bilkent, 06800 Ankara, Turkey. <sup>2</sup>IMCN/NAPS, Université Catholique de Louvain (UCLouvain), 1348 Louvain-la-Neuve, Belgium. <sup>3</sup>Department of Physics, Bilkent University, Bilkent, 06800 Ankara, Turkey. <sup>4</sup>James Watt School of Engineering, University of Glasgow, Glasgow G12 8LT, UK. ✉email: kasirga@unam.bilkent.edu.tr

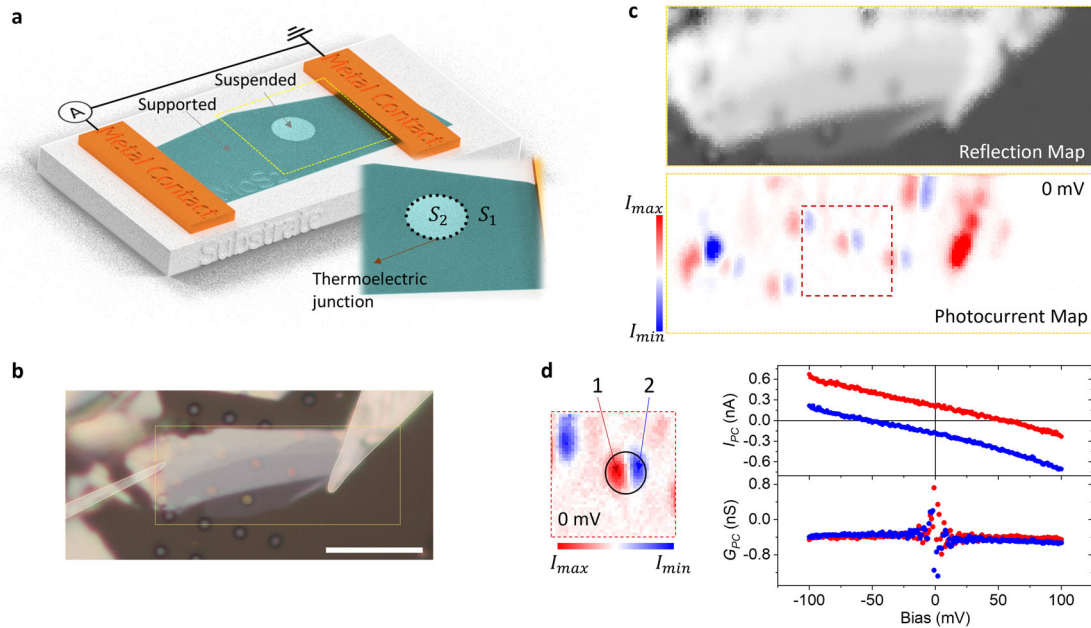


**Fig. 1** **Single-material thermoelectric junction.** **a** Schematic of a substrate-engineered device: a MoS<sub>2</sub> flake is suspended over a circular hole drilled in the substrate. Metal contacts are used for scanning photocurrent microscopy (SPCM), scanning thermal gate microscopy (SThGM) and I–V measurements. The inset shows a magnification of the area indicated by the dashed yellow square, where Seebeck coefficients of supported and suspended parts are labeled with S<sub>1</sub> and S<sub>2</sub>, respectively. **b** Optical microscope image of a multi-layered device over circular holes with indium contacts, marked with gray overlays. Scale bar: 10 μm. **c** SPCM reflection map and the corresponding open-circuit photocurrent map acquired from the yellow dashed rectangle in (b) with 532 nm laser. {I<sub>min</sub>, I<sub>max</sub>} = –0.5, 0.5 nA. **d** Photocurrent map from the reflection image. Black circle is the position of the hole determined from the reflection image. Right panel shows the photocurrent, I<sub>PC</sub> vs bias taken from point 1 (red dots) and point 2 (blue dots) over the suspended part of the crystal marked on the left panel. Lower graph is the derived photoconductance, G<sub>PC</sub> vs. bias.

which are suitable for achieving Ohmic contacts to MoS<sub>2</sub><sup>24,25</sup> (gold-contacted device measurements are shown in Supplementary Note 2 and Supplementary Fig. 1). A typical device is shown in Fig. 1b. We then used scanning photocurrent microscopy to locally heat up the junction with a focused laser beam and to measure the photothermoelectric current that is generated (see “Methods” for experimental details). Figure 1c shows the greyscale reflection intensity map and the corresponding photocurrent distribution over the device. For the few-layer suspended MoS<sub>2</sub> devices, we observe a bipolar photoresponse at the junctions between the supported and the suspended part of the crystal. The spatial distribution of the signal agrees well with the finite element analysis simulations given in Supplementary Note 3 (and Supplementary Fig. 2 therein) and suggests the formation of a thermoelectric junction. When applying a voltage bias  $V$  to the junction, the photocurrent,  $I_{PC}$  changes linearly with bias, while the photoconductance,  $G_{PC} = \frac{I_{PC} - I_{PC}^0}{V}$  ( $I_{PC}^0, I_{PC}^0$ : photocurrent under  $V$  and 0 mV bias, respectively) stays constant (Fig. 1d). Such bias-independent photoconductance is typically an indication for a photothermoelectric nature of the observed signal<sup>21,23,26–28</sup>. Although we propose that the photocurrent in substrate-engineered MoS<sub>2</sub> devices is dominated by the photothermal effect (PTE)<sup>29,30</sup>, other possible mechanisms have been reported that may lead to a photovoltaic response. These include (1) strain-related effects such as strain modulation of materials properties and flexo-photovoltaic effect<sup>13</sup>, and (2) substrate proximity-related effects that forms a built-in electric field<sup>31</sup>.

### Thermoelectric origin of the photocurrent

Next, we present experimental evidence for a thermoelectric origin of the observed photocurrent. To this end, we employed scanning thermal gate microscopy (SThGM), where a hot AFM tip heats up the junction locally while the resulting voltage build-up on the

devices is recorded (see “Methods”). Since no laser-illumination of the sample is required in this method, it can be used to ultimately exclude photovoltaic effects. Figure 2 compares SPCM and SThGM maps of the same holes. We observed the same bipolar signals in the suspended regions with both experimental methods. Thanks to its sub-100 nm lateral resolution, SThGM further allows us to observe local variations of the thermovoltage in supported MoS<sub>2</sub> that can be attributed to charge puddles induced by local doping via the substrate<sup>32–34</sup>. We confirmed that the SThGM signal disappears when no power is dissipated in the probe heater, which rules out parasitic effects induced by the laser used for AFM feedback. Furthermore, SThGM allows us to estimate the magnitude of the local Seebeck coefficient variations. Using the probe-calibration data, we obtain a value of  $\Delta S = 72 \pm 10 \mu\text{V K}^{-1}$  (See Supplementary Note 4). Despite the uncertainties regarding the real sample temperature, the obtained  $\Delta S$  value is very close to the theoretically predicted value.

To understand why suspending MoS<sub>2</sub> alters its Seebeck coefficient, we first would like to discuss the possibility of strain-induced changes in the material’s properties. MoS<sub>2</sub>, like graphene, is nominally compressed when deposited on a substrate<sup>35–38</sup>. Upon suspending the crystals, the free-standing part either adheres to the sidewalls of the hole and dimples or bulges. As a result, the strain might be present in the free-standing part of the crystal. Strain can affect both the bandgap and the Seebeck coefficient of MoS<sub>2</sub>. The indirect optical gap is modulated by  $-110 \text{ meV}/\%$ -strain for a trilayer MoS<sub>2</sub><sup>35,39</sup>. Ab initio studies show a  $\sim 10\%$  decrease in the Seebeck coefficient of monolayer MoS<sub>2</sub> per 1% tensile strain<sup>40</sup>. To estimate the biaxial strain, we performed atomic force microscopy (AFM) height trace mapping on the samples. Most samples, regardless of the geometry of the hole, exhibit slight bulging of a few nanometers. For the MoS<sub>2</sub> flakes suspended on the circular holes in the device shown in Fig. 3a, the bulge height is  $\delta t \approx 25 \text{ nm}$ . The SPCM map for the

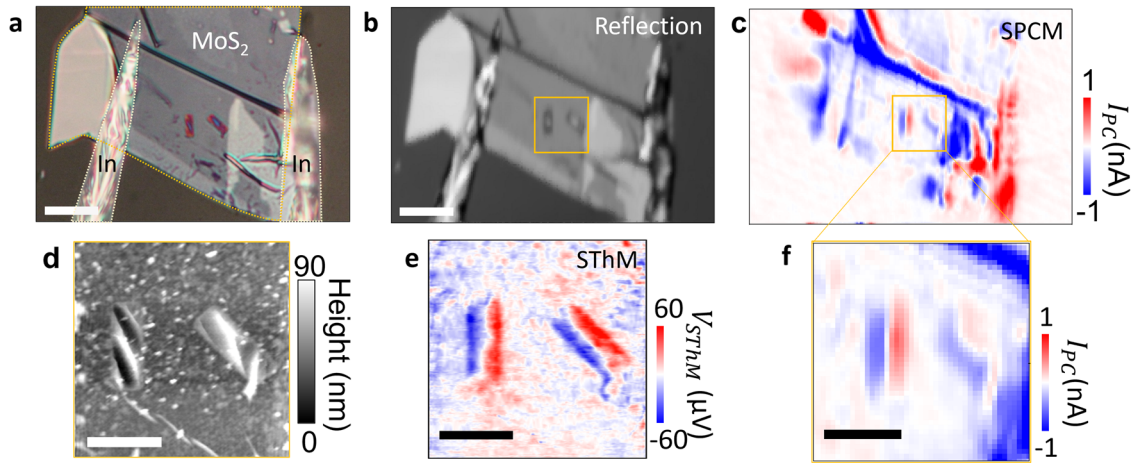


**Fig. 2 Comparison of SPCM and SThGM measurements.** **a** Optical micrograph of the device. Scale bar is 10  $\mu\text{m}$ . **b** SPCM reflection map and **c** photocurrent map of the device shown in **(a)**. Scale bar: 10  $\mu\text{m}$ . The yellow rectangle indicates the region that was investigated by SThGM in **(d)** (AFM height map) and **e** (SThGM thermovoltage map). **f** SPCM map of the same region excerpted from the map given in **(c)**. Color scale is the same as in **(c)**. Scale bars in **(d–f)**: 3  $\mu\text{m}$ .

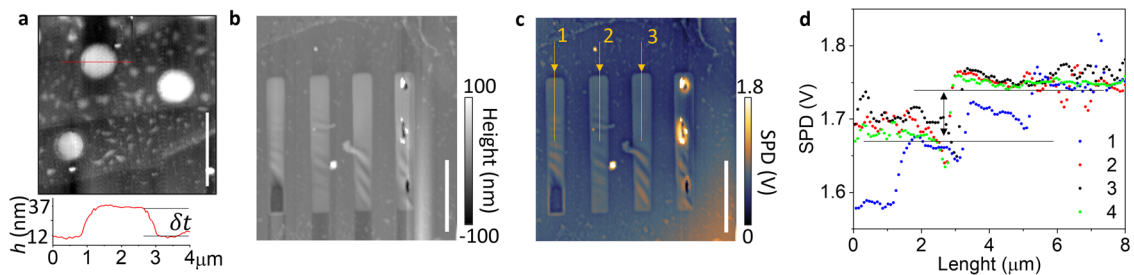


**Fig. 3 Surface topography and surface potential difference.** **a** AFM height trace map of a device suspended over circular holes show a bulge of  $\delta t \approx 25$  nm. The lower panel shows the height trace over the red line shown on the map. SPCM map for the hole is given in Fig. 1d. Scale bar: 4  $\mu\text{m}$ . **b** AFM height trace map of the sample shows the bulged and dimpled parts of the flake. Scale bar: 4  $\mu\text{m}$ . **c** KPFM map of the sample shows the variation in the surface potential. Scale bar: 4  $\mu\text{m}$ . **d** Line traces taken along the numbered lines in **(c)**. Direction of the arrows in **(c)** indicates the direction of the line plot.

sample is shown in Fig. 1d. Similar  $\delta t$  values were measured for other devices. The biaxial strain can then be calculated using a uniformly loaded circular membrane model and is as low as 0.0025%<sup>41</sup>. Such a small strain on MoS<sub>2</sub> is not sufficient to induce a significant change in bandgap or Seebeck coefficient<sup>13,42,43</sup>. Further experimental evidence regarding limited strain contribution on the observed bipolar response based on Raman mapping of various samples is provided in Supplementary Notes 5 and 6<sup>44,45</sup>. We also would like to note that the observed response has no polarization dependence, again as discussed in Supplementary Note 7.

Next, we consider the substrate-induced changes on the material properties. The presence or the absence of the substrate can cause enhanced or diminished optical absorption due to the screening effects, Fermi level pinning<sup>46</sup> and charges donated by the substrate<sup>7,47</sup>. More significantly, the doping effect due to the trapped charges at the interface with the substrate can locally gate the MoS<sub>2</sub> and modify the number of charge carriers<sup>48</sup> and thus its Seebeck coefficient. To investigate the electrostatic impact of the substrate on the MoS<sub>2</sub> membrane, we investigated the surface potential difference (SPD) on devices using Kelvin Probe Force Microscopy (KPFM). SPD can provide an insight on the band bending of the MoS<sub>2</sub> due to the substrate effects<sup>49</sup>. Figure 3b–d shows the AFM height trace map and the uncalibrated SPD map of the sample. SPD across the supported and suspended part of the flake is on the order of 50 mV. This shift in the SPD value hints that there is a slight change in the Fermi level of the suspended part with respect to the supported part of the crystal. The same type of charge carriers is dominant on both sides of the junction

formed by the suspended and supported parts of the crystal. The band structure formed by such a junction in zero bias cannot be used in the separation of photoinduced carriers<sup>50</sup>; however, it can lead to the formation of a thermoelectric junction<sup>11,51</sup>. This is in line with the SThGM measurements.

### Controlling the substrate effect via electric field

In the remainder of the paper, we aim at controlling the electrostatics that is responsible for the formation of a thermoelectric junction. Charge transport in MoS<sub>2</sub> is dominated by electrons due to unintentional doping<sup>18,52</sup>. Modulating the density and the type of free charge carriers can be done by applying a gate voltage  $V_G$  to the junction<sup>53</sup>. This significantly modifies the magnitude and the sign of the Seebeck coefficient as demonstrated in previous studies<sup>16,29,30,54</sup>. The Mott relation<sup>55</sup> can be used to model the Seebeck coefficient as a function of  $V_G$ :

$$S = \frac{\pi^2 k_B^2 T}{3e} \frac{1}{R} \frac{dR}{dV_G} \frac{dV_G}{dE} \Big|_{E=E_F} \quad (2)$$

Here,  $T$  is the temperature,  $k_B$  is the Boltzmann constant,  $e$  is the electron's charge,  $R$  is the device resistance,  $E_F$  is the Fermi energy, and  $E$  is the energy.

Since hole transport is limited due to substrate-induced Fermi level pinning on SiO<sub>2</sub> supported MoS<sub>2</sub> field-effect devices<sup>46</sup> to observe the sign inversion of the Seebeck coefficient (see Supplementary Note 6 for measurements on device fabricated on SiO<sub>2</sub> and Al<sub>2</sub>O<sub>3</sub>-coated SiO<sub>2</sub>) we followed an alternative approach to emulate suspension: we fabricated heterostructure devices where

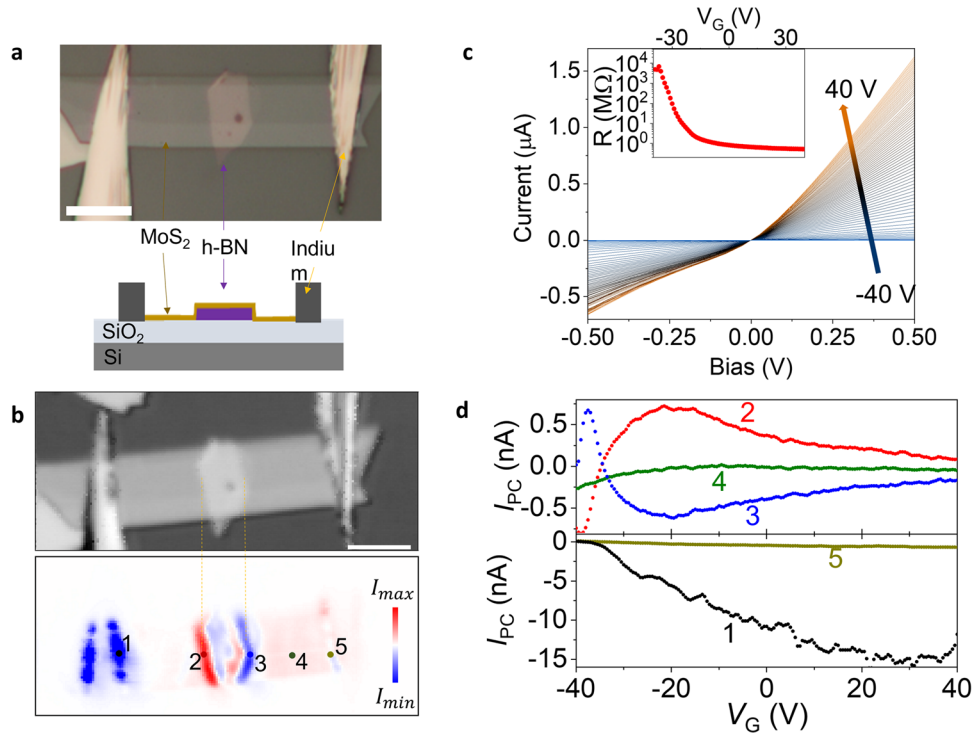


**Fig. 4 Gate modulation of the thermoelectric response.** **a** Optical micrograph of a Si back-gated MoS<sub>2</sub> device partially placed over h-BN. Its cross-sectional schematic is shown in the lower panel. Scale bar: 10 μm. **b** SPCM reflection map and the photocurrent map of the device shown in (a).  $I_{\max} = 3$  nA and  $I_{\min} = -3$  nA. Scale bar: 10 μm. **c** Current–Voltage graph versus  $V_G$  from  $-40$  to  $40$  V. Inset shows the resistance versus  $V_G$ . **d**  $I_{PC}$  vs.  $V_G$  recorded at the points marked in the SPCM map in (b).

the crystal is partially supported by hexagonal boron nitride (h-BN). h-BN is commonly used to encapsulate two-dimensional materials thanks to its hydrophobic and atomically smooth surface. This leads to less unintentional doping due to the interfacial charge trapping and reduced electron scattering<sup>7,56,57</sup>. A  $\sim 10$  ML MoS<sub>2</sub> is placed over a 10-nm thick h-BN crystal to form a double-junction device (see Supplementary Note 7 for a single-junction device), and indium contacts are placed over the MoS<sub>2</sub>. The device is on 1 μm thick oxide-coated Si substrate where Si is used as the back-gate electrode. Figure 4a shows the optical micrograph of the device and its schematic. The presence of h-BN modifies the SPD by 80 mV—a value very similar to the values we find for suspended devices (see Supplementary Note 7)—which is consistent with the relative n-doping by the h-BN substrate<sup>31,56</sup>. We, therefore, attribute this difference to the Fermi level shift due to the difference in interfacial charge doping by the different substrates.

Figure 4b shows the SPCM map under zero gate voltage. We observe a bipolar photocurrent signal from the junctions between h-BN and SiO<sub>2</sub> supported MoS<sub>2</sub>. Raman mapping (see Supplementary Fig. 12) reveals a slight intensity decrease and a small shift of the A<sub>1g</sub> peak over the h-BN-supported part of the MoS<sub>2</sub>. This is consistent with the stiffening of the Raman mode due to the higher degree of charged impurities in SiO<sub>2</sub> as compared to h-BN<sup>7</sup>. By applying a gate voltage to the device, its resistance can be tuned significantly as free charges are depleted (Fig. 4c). Under large positive gate voltages, the  $I$ - $V$  characteristic becomes asymmetric. To investigate the dependence of the photocurrent on carrier type and concentration, the laser is held at specific positions on the device as marked in Fig. 4d, and the gate is swept from positive to negative voltages with respect to the ground terminal. For positive gate voltages, the magnitude of the photoresponse from both junctions, between h-BN and SiO<sub>2</sub> supported MoS<sub>2</sub>, (points 2 and 3) decreases. When a negative gate voltage is applied, the magnitude of the photoresponse at both junctions increases by almost a factor of two at  $V_G = -21.5$  V.

Once this maximum is reached, the amplitude of the photocurrent at both points decreases and has the same value as the photocurrent generated over the MoS<sub>2</sub> (point 4) at  $V_G = -34.5$  V.

These observations can be qualitatively explained as follows: at a gate voltage of  $V_G = -34.5$  V, the majority charge carrier type in the h-BN supported part changes from electrons to holes. As a consequence, the Seebeck coefficients of MoS<sub>2</sub> resting on h-BN and SiO<sub>2</sub>, respectively, become similar, which leads to  $\Delta S \approx 0$ , and curves 2, 3, and 4 in Fig. 4d cross. The photocurrent signal recorded near the indium contacts (points 1 and 5) decreases non-monotonically with decreasing  $V_G$  and reaches zero at  $V_G = -40$  V. This shows that the photoresponse mechanism at the Indium-MoS<sub>2</sub> junction is not solely due to the Seebeck effect.

In conclusion, we demonstrated that substrate engineering can be used to generate a thermoelectric junction in atomically thin MoS<sub>2</sub> devices. Similar strategies can be employed in other low-dimensional materials that exhibit large and tunable Seebeck coefficients. This might in particular be promising at low temperature where effects like band-hybridization and Kondo scattering can produce a very strong photothermoelectric effect<sup>9</sup>.

## METHODS

### Scanning photocurrent microscopy

SPCM setup is a commercially available setup from LST Scientific Instruments Ltd., which offers a compact scanning head with easily interchangeable lasers. Two SR-830 Lock-in amplifiers are employed, one for the reflection map and the other for the photocurrent/voltage measurements. In the main text we reported the photocurrent (a measurement of the photovoltage is given in Supplementary Note 9). The incident laser beam is chopped at a certain frequency and focused onto the sample through a 40x objective. The electrical response is collected through gold probes pressed on the electrical contacts of the devices and the signal is amplified by a lock-in amplifier set to the

chopping frequency of the laser beam. Although various wavelengths (406, 532, 633 nm) are employed for the measurements, unless otherwise stated we used 532 nm in the experiments reported in the main text (see Supplementary Fig. 12 for SPCM measurements with different wavelengths). All the excitation energies are above the indirect bandgap of the few-layer MoS<sub>2</sub>. We showed that devices are very durable even when they are kept under ambient for 23 months. We measured the device reported in Fig. 1 after 23 months and obtained very similar magnitudes for the photoresponse (see Supplementary Note 10).

### Scanning thermal microscopy

Scanning Thermal Microscopy measurements were performed with a Dimension Icon (Bruker) AFM under ambient conditions. The probe used in the experiments is VITA-DM-GLA-1 made of a palladium heater on a silicon nitride cantilever and tip. The radius is typically in the order of 25–40 nm. The heater is part of a modified Wheatstone bridge and is driven by a combined 91 kHz AC and DC bias, as reported elsewhere. The signal is detected via a SR-830 lock-in amplifier and fed in the AFM controller. This signal monitors the probe temperature and thus allows to locally map the thermal conductance of the sample. In this work, the power supplied to the probe gives rise to a 45 K excess temperature.

While the probe is scanning the sample, we measure the voltage drop across the device using a low-noise preamplifier (SR 560). This voltage is created by the local heating induced by the hot SThM tip. It is then fed also to the AFM controller and recorded simultaneously. In this study, the thermovoltage measurements were performed without modulating the heater power. We note that it is also possible to generate similar maps by varying the heater temperature and detecting thermovoltage via lock-in detection.

### DATA AVAILABILITY

Source data is available from the corresponding author upon request.

Received: 19 December 2022; Accepted: 18 May 2023;

Published online: 26 May 2023

### REFERENCES

- Chen, J. H. et al. Charged-impurity scattering in graphene. *Nat. Phys.* **4**, 377–381 (2008).
- Zhang, Y., Brar, V. W., Girit, C., Zettl, A. & Crommie, M. F. Origin of spatial charge inhomogeneity in graphene. *Nat. Phys.* **5**, 722–726 (2009).
- Wang, Q. H. et al. Understanding and controlling the substrate effect on graphene electron-transfer chemistry via reactivity imprint lithography. *Nat. Chem.* **4**, 724–732 (2012).
- Bao, W., Cai, X., Kim, D., Sridhara, K. & Fuhrer, M. S. High mobility ambipolar MoS<sub>2</sub> field-effect transistors: Substrate and dielectric effects. *Appl. Phys. Lett.* **102**, 042104 (2013).
- Robinson, B. J. et al. Structural, optical and electrostatic properties of single and few-layers MoS<sub>2</sub>: effect of substrate. *2D Mater.* **2**, 015005 (2015).
- Wang, L., Nilsson, Z. N., Tahir, M., Chen, H. & Sambur, J. B. Influence of the substrate on the optical and photo-electrochemical properties of monolayer MoS<sub>2</sub>. *ACS Appl. Mater. Interfaces* **12**, 15034–15042 (2020).
- Buscema, M., Steele, G. A., van der Zant, H. S. J. & Castellanos-Gomez, A. The effect of the substrate on the Raman and photoluminescence emission of single-layer MoS<sub>2</sub>. *Nano Res.* **7**, 561–571 (2014).
- Sercombe, D. et al. Optical investigation of the natural electron doping in thin MoS<sub>2</sub> films deposited on dielectric substrates. *Sci. Rep.* **3**, 1–6 (2013).
- Wu, J. et al. Large enhancement of thermoelectric performance in MoS<sub>2</sub>/h-BN heterostructure due to vacancy-induced band hybridization. *Proc. Natl Acad. Sci. USA* **117**, 13929–13936 (2020).
- Herring, C. Theory of the thermoelectric power of semiconductors. *Phys. Rev.* **96**, 1163–1187 (1954).
- Ng, H. K., Chi, D. & Hippalgaonkar, K. Effect of dimensionality on thermoelectric powerfactor of molybdenum disulfide. *J. Appl. Phys.* **121**, 204303 (2017).

- Cui, X. et al. Multi-terminal transport measurements of MoS<sub>2</sub> using a van der Waals heterostructure device platform. *Nat. Nanotechnol.* **10**, 534–540 (2015).
- Jiang, J. et al. Flexo-photovoltaic effect in MoS<sub>2</sub>. *Nat. Nanotechnol.* **16**, 894–901 (2021).
- Rice, C. et al. Raman-scattering measurements and first-principles calculations of strain-induced phonon shifts in monolayer MoS<sub>2</sub>. *Phys. Rev. B Condens. Matter Mater. Phys.* **87**, 081307 (2013).
- Hippalgaonkar, K. et al. High thermoelectric power factor in two-dimensional crystals of MoS<sub>2</sub>. *Phys. Rev. B* **95**, 115407 (2017).
- Kayyalha, M., Maassen, J., Lundstrom, M., Shi, L. & Chen, Y. P. Gate-tunable and thickness-dependent electronic and thermoelectric transport in few-layer MoS<sub>2</sub>. *J. Appl. Phys.* **120**, 134305 (2016).
- Liu, L., Lu, Y. & Guo, J. On monolayer MoS<sub>2</sub> field-effect transistors at the scaling limit. *IEEE Trans. Electron Devices* **60**, 4133–4139 (2013).
- Dagan, R. et al. Two-dimensional charge carrier distribution in MoS<sub>2</sub> monolayer and multilayers. *Appl. Phys. Lett.* **114**, 101602 (2019).
- Chae, W. H., Cain, J. D., Hanson, E. D., Murthy, A. A. & Dravid, V. P. Substrate-induced strain and charge doping in CVD-grown monolayer MoS<sub>2</sub>. *Appl. Phys. Lett.* **111**, 143106 (2017).
- Castellanos-Gomez, A. et al. Deterministic transfer of two-dimensional materials by all-dry viscoelastic stamping. *2D Mater.* **1**, 011002 (2014).
- Mehmood, N., Rasouli, H. R., Çakıroğlu, O. & Kasirga, T. S. Photocurrent generation in a metallic transition-metal dichalcogenide. *Phys. Rev. B* **97**, 195412 (2018).
- Rasouli, H. R. et al. Electric-field-induced reversible phase transitions in a spontaneously ion-intercalated 2D metal oxide. *Nano Lett.* **21**, 3997–4005 (2021).
- Razeghi, M., Üstünçelik, M., Shabani, F., Demir, H. V. & Kasirga, T. S. Plasmon-enhanced photoresponse of single silver nanowires and their network devices. *Nanoscale Horiz.* **7**, 396–402 (2022).
- Kim, B.-K. et al. Origins of genuine Ohmic van der Waals contact between indium and MoS<sub>2</sub>. *npj 2D Mater. Appl.* **5**, 9 (2021).
- Wang, Y. et al. Van der Waals contacts between three-dimensional metals and two-dimensional semiconductors. *Nature* **568**, 70–74 (2019).
- Kasirga, T. S. *Thermal Conductivity Measurements in Atomically Thin Materials and Devices* (Springer Singapore, 2020).
- Kasirga, T. S. et al. Photoresponse of a strongly correlated material determined by scanning photocurrent microscopy. *Nat. Nanotechnol.* **7**, 723–727 (2012).
- Çakıroğlu, O. et al. Thermal conductivity measurements in nanosheets via bolometric effect. *2D Mater.* **7**, 035003 (2020).
- Buscema, M. et al. Large and tunable photothermoelectric effect in single-layer MoS<sub>2</sub>. *Nano Lett.* **13**, 358–363 (2013).
- Zhang, Y. et al. Photothermoelectric and photovoltaic effects both present in MoS<sub>2</sub>. *Sci. Rep.* **5**, 1–7 (2015).
- Utama, M. I. B. et al. A dielectric-defined lateral heterojunction in a monolayer semiconductor. *Nat. Electron.* **2**, 60–65 (2019).
- Harzheim, A., Evangelii, C., Kolosov, O. V. & Gehring, P. Direct mapping of local Seebeck coefficient in 2D material nanostructures via scanning thermal gate microscopy. *2D Mater.* **7**, 041004 (2020).
- Spiege, J. et al. Quantifying thermal transport in buried semiconductor nanostructures: via cross-sectional scanning thermal microscopy. *Nanoscale* **13**, 10829–10836 (2021).
- Spiege, J. et al. Improving accuracy of nanothermal measurements via spatially distributed scanning thermal microscope probes. *J. Appl. Phys.* **124**, 015101 (2018).
- Lloyd, D. et al. Band gap engineering with ultralarge biaxial strains in suspended monolayer MoS<sub>2</sub>. *Nano Lett.* **16**, 5836–5841 (2016).
- Bertolazzi, S., Brivio, J. & Kis, A. Stretching and breaking of ultrathin MoS<sub>2</sub>. *ACS Nano* **5**, 9703–9709 (2011).
- Lee, C., Wei, X., Kysar, J. W. & Hone, J. Measurement of the elastic properties and intrinsic strength of monolayer graphene. *Science* **321**, 385–388 (2008).
- Castellanos-Gomez, A. et al. Elastic properties of freely suspended MoS<sub>2</sub> nanosheets. *Adv. Mater.* **24**, 772–775 (2012).
- Li, Z. et al. Efficient strain modulation of 2D materials via polymer encapsulation. *Nat. Commun.* **11**, 1151 (2020).
- Dimple, Jena, N. & De Sarkar, A. Compressive strain induced enhancement in thermoelectric-power-factor in monolayer MoS<sub>2</sub> nanosheet. *J. Phys. Condens. Matter* **29**, 225501 (2017).
- Fichter, W. B. Some solutions for the large deflections of uniformly loaded circular membranes. *NASA Tech. Pap* **3658**, 13–16 (1997).
- Yang, M. M., Kim, D. J. & Alexe, M. Flexo-photovoltaic effect. *Science* **360**, 904–907 (2018).
- Huang, Y. et al. An efficient route to prepare suspended monolayer for feasible optical and electronic characterizations of two-dimensional materials. *InfoMat* **4**, e12274 (2022).
- Lee, J. U. et al. Strain-shear coupling in bilayer MoS. *Nat. Commun.* **8**, 1–7 (2017).
- Çakıroğlu, O., Island, J. O., Xie, Y., Frisenda, R. & Castellanos-Gomez, A. An automated system for strain engineering and straintronics of 2D materials. *Adv. Mater. Technol.* **8**, 2201091 (2023).

46. Mootheri, V. et al. Understanding ambipolar transport in MoS<sub>2</sub> field effect transistors: the substrate is the key. *Nanotechnology* **32**, 135202 (2021).
47. Drüppel, M., Deilmann, T., Krüger, P. & Rohlfing, M. Diversity of trion states and substrate effects in the optical properties of an MoS<sub>2</sub> monolayer. *Nat. Commun.* **8**, 1–7 (2017).
48. Lu, C. P., Li, G., Mao, J., Wang, L. M. & Andrei, E. Y. Bandgap, mid-gap states, and gating effects in MoS<sub>2</sub>. *Nano Lett.* **14**, 4628–4633 (2014).
49. Ochedowski, O. et al. Effect of contaminations and surface preparation on the work function of single layer MoS<sub>2</sub>. *Beilstein J. Nanotechnol.* **5**, 291–297 (2014).
50. Sun, D. et al. Ultrafast hot-carrier-dominated photocurrent in graphene. *Nat. Nanotechnol.* **7**, 114–118 (2012).
51. Lee, C., Hong, J., Lee, W. R., Kim, D. Y. & Shim, J. H. Density functional theory investigation of the electronic structure and thermoelectric properties of layered MoS<sub>2</sub>, MoSe<sub>2</sub> and their mixed-layer compound. *J. Solid State Chem.* **211**, 113–119 (2014).
52. Siao, M. D. et al. Two-dimensional electronic transport and surface electron accumulation in MoS<sub>2</sub>. *Nat. Commun.* **9**, 1–12 (2018).
53. Jahangir, I., Koley, G. & Chandrashekar, M. V. S. Back gated FETs fabricated by large-area, transfer-free growth of a few layer MoS<sub>2</sub> with high electron mobility. *Appl. Phys. Lett.* **110**, 182108 (2017).
54. Dobusch, L. et al. Electric field modulation of thermovoltage in single-layer MoS<sub>2</sub>. *Appl. Phys. Lett.* **105**, 253103 (2014).
55. Ashcroft, N. & Mermin, D. *Solid State Physics* (Thomson Learning Inc., 1976).
56. Joo, M. K. et al. Electron excess doping and effective Schottky barrier reduction on the MoS<sub>2</sub>/h-BN heterostructure. *Nano Lett.* **16**, 6383–6389 (2016).
57. Li, L. et al. Raman shift and electrical properties of MoS<sub>2</sub> bilayer on boron nitride substrate. *Nanotechnology* **26**, 295702 (2015).

## ACKNOWLEDGEMENTS

T.S.K. acknowledges support from TUBITAK under grant no: 121F366.

## AUTHOR CONTRIBUTIONS

T.S.K. designed and conceived the experiments. T.S.K. and P.G. prepared the manuscript. M.R. fabricated devices, performed the experiment, and analyzed the results. D.P. prepared the substrates, performed simulations, and helped with the experiments. O.O. performed the AFM and KPFM measurements and A.S. performed some of the earlier measurements. U.B. prepared some samples and performed

polarization-dependent measurements. J.S., Y.H., and P.G. performed the SThGM measurements and analyzed the results. P.S.D. and J.M.R.W. contributed to discussions on the implementation of VITA-DM-GLA-1 SThM probes. All authors discussed the results and reviewed the final version of the manuscript.

## COMPETING INTERESTS

The authors declare no competing interests.

## ADDITIONAL INFORMATION

**Supplementary information** The online version contains supplementary material available at <https://doi.org/10.1038/s41699-023-00406-z>.

**Correspondence** and requests for materials should be addressed to T. Serkan Kasirga.

**Reprints and permission information** is available at <http://www.nature.com/reprints>

**Publisher's note** Springer Nature remains neutral with regard to jurisdictional claims in published maps and institutional affiliations.



**Open Access** This article is licensed under a Creative Commons Attribution 4.0 International License, which permits use, sharing, adaptation, distribution and reproduction in any medium or format, as long as you give appropriate credit to the original author(s) and the source, provide a link to the Creative Commons license, and indicate if changes were made. The images or other third party material in this article are included in the article's Creative Commons license, unless indicated otherwise in a credit line to the material. If material is not included in the article's Creative Commons license and your intended use is not permitted by statutory regulation or exceeds the permitted use, you will need to obtain permission directly from the copyright holder. To view a copy of this license, visit <http://creativecommons.org/licenses/by/4.0/>.

© The Author(s) 2023